A remote sensing method for mapping alpine grasslines based on graph-cut

Running title: Remotely sensing of alpine grasslines

Licong Liu[1], Jin Chen[1], Miaogen Shen[1*], Xuehong Chen[1], Ruyin Cao[2], Xin Cao[1], Xihong Cui[1], Wei Yang[3], Xiaolin Zhu[4], Le Li[5], Yanhong Tang[6]

ORCID IDs:

Licong Liu: 0009-0001-0067-3411;

Jin Chen:

Miaogen Shen: 0000-0001-5742-8807

Xuehong Chen:

Ruyin Cao: 0000-0002-8122-9696

Xin Cao: 0000-0001-5789-7582

Xihong Cui: 0000-0002-5590-1995

Wei Yang:

Xiaolin Zhu: 0000-0001-6967-786X

Le Li:

Yanhong Tang: 0000-0001-7207-1965

[1]State Key Laboratory of Earth Surface Processes and Resource Ecology, Faculty of Geographical Science, Beijing Normal University, Beijing, China

[2]School of Resources and Environment, University of Electronic Science and Technology of China, Chengdu, China

[3]Center for Environmental Remote Sensing, Chiba University, Chiba, Japan

[4]Department of Land Surveying and Geo-Informatics, The Hong Kong Polytechnic University, Hong Kong, China

[5]School of Management, Guangdong University of Technology, Guangzhou, China

[6]College of Urban and Environmental Sciences, Peking University, Beijing, China

*Author for correspondence, shen.miaogen@gmail.com

Abstract

Climate change has induced substantial shifts in vegetation boundaries such as alpine treelines and shrublines, with widespread ecological and climatic influences. However, spatial and temporal changes in the upper elevational limit of alpine grasslands ("alpine grasslines") are still poorly understood due to lack of field observations and remote sensing estimates. In this study, taking the Tibetan Plateau as an example, we propose a novel method for automatically identifying alpine grasslines from multi-source remote sensing data and determining their positions at 30-m spatial resolution. We first identified 2895 mountains potentially having alpine grasslines. On each mountain, we identified a narrow area around the upper elevational limit of alpine grasslands where the alpine grassline was potentially located. Then, we used linear discriminant analysis to adaptively generate from Landsat reflectance features a synthetic feature that maximized the difference between vegetated and unvegetated pixels in each of these areas. After that, we designed a graph-cut algorithm to integrate the advantages of the Otsu and Canny approaches, which was used to determine the precise position of the alpine grassline from the synthetic feature image. Validation against alpine grasslines visually interpreted from a large number of high-spatial-resolution images showed a high level of accuracy (R^2, 0.99 and 0.98; mean absolute error, 22.6 and 36.2 m, versus drone and PlanetScope images, respectively). Across the Tibetan Plateau, the alpine grassline elevation ranged from 4038 to 5380 m (5th–95th percentile), lower in the northeast and southeast and higher in the southwest. This study provides a method for remotely sensing alpine grasslines for the first-time at large scale and lays a foundation for investigating their responses to climate

change.

Key words: alpine grassline, climate change, edge detection, graph-cut, Landsat, Tibetan Plateau

1. Introduction

Rising temperatures associated with climate change have caused substantial shifts in species' ranges and vegetation distributions (I. C. Chen, Hill, Ohlemuller, Roy, & Thomas, 2011; Kelly & Goulden, 2008; Lenoir, Gégout, Marquet, de Ruffray, & Brisse, 2008; Zong et al., 2022). These changes alter community and ecosystem structure and function and land surface processes, which exert feedback to the climate system (Chapin et al., 2000; Myers-Smith et al., 2011; Zhang et al., 2013). In past decades, remarkable shifts of species' ranges toward higher latitudes and altitudes, induced by warming, have been observed (Bobrowski, Gerlitz, & Schickhoff, 2017; I. C. Chen et al., 2011; Dolezal et al., 2016), although downhill shifts due to moisture conditions have been observed in a few cases (Crimmins, Dobrowski, Greenberg, Abatzoglou, & Mynsberge, 2011). Similarly, local-scale movements of vegetation boundaries have also been recorded, including forest expansion in the Arctic (Zhang et al., 2013) and upward shifts of alpine treelines and shrublines on the Tibetan Plateau (Liang et al., 2016; Y. Wang et al., 2021). Even though grasslands are widely distributed in alpine regions of the world, and their distribution is highly sensitive to climate change (Compagnoni et al., 2021; Shen et al., 2022; Y. Wang et al., 2021), spatial and temporal changes in the upper elevational range of

alpine grasslands (hereafter “alpine grasslines”) remain poorly understood.

The lack of understanding of alpine grassline changes originates from a lack of field observations and remote sensing retrievals of grassline elevations. For example, Anderson et al. (2020) used a Landsat Normalized Difference Vegetation Index (NDVI, a proxy of vegetation coverage or green biomass) threshold of ≥ 0.1 to show a general expansion of vegetation, possibly including an uphill shift of the alpine grassline, in the subnival Hindu Kush Himalaya between 1993 and 2018. In contrast, no increase in the NDVI from 2000 to 2014 was reported at six sites across the Tibetan Plateau that included the upper elevational limit of grassland (Huang, He, Chen, & Wang, 2018). These different results suggest that an NDVI threshold of 0.1 cannot be effectively used to discriminate between the presence and absence of vegetation, because the NDVI for bare soil can vary between 0 and 0.4 (Montandon & Small, 2008). Therefore, given the lack of ground observations, it is necessary to develop a method to identify alpine grasslines from satellite data. By using the more than 40 years of archived satellite data (e.g., Landsat images), such a method would allow us to characterize spatial and temporal changes in alpine grasslines and their drivers.

Previously, boundaries between two land cover types (such as alpine treelines—between forest and grassland and vegetation lines—between vegetation and bare land) have been determined by using a universal NDVI threshold, estimating a single feature such as tree cover, or directly identifying the edges of a land cover type (Anderson et al., 2020; X Wang et al., 2022; Zou et al., 2023). Similar to the method based on a universal NDVI threshold (Anderson et al., 2020), a tree coverage threshold of 10% was used to determine the treelines in the

Himalayas from a tree coverage product based on Landsat images (Hansen et al., 2013; X Wang et al., 2022). Different from these methods using pre-determined single threshold, land cover product from satellite images was used to mapping the upper elevational limits of vegetations globally (Zou et al., 2023). However, these methods can suffer from different NDVI thresholds (Montandon & Small, 2008) for distinguishing between bare land and vegetation, bias in the estimation of tree cover (Hansen et al., 2013), or errors in the land cover product (Zanaga et al., 2022). Unlike these methods, there are studies in which the Otsu algorism was used to estimate the position of alpine treelines in mountain regions from Landsat NDVI (He et al., 2020). However, the Otsu algorism could be affected by the use of single threshold and determination of such threshold relies on the NDVI histograms that discards the gradient of NDVI, making it difficult to accurately identify the treelines.

Therefore, taking the Tibetan Plateau as an example, we aimed to use satellite data to map alpine grasslines. The Tibetan Plateau is an ideal experimental area for the development and evaluation of a method for identifying alpine grasslines. First, alpine grasslands on the Tibetan Plateau cover an area of 1.5×10^6 km^2, with latitudinal, longitudinal, and elevation spans of about 15°, 30°, and 3000 m (An et al., 2018; Shen et al., 2022; C. Wang et al., 2015), respectively. Further, climate conditions on the plateau are highly heterogeneous spatially; the mean annual growing season temperature and precipitation range from < 0 °C to > 20 °C and from <200 mm to >1000 mm, respectively (Cong et al., 2017). Thus, alpine grasslines can be expected to show high spatial variability. Finally, as the highest mountainous region in the world with varied grassland ecosystems, information on alpine grasslines on the Tibetan

Plateau is fundamental to understanding the responses of alpine ecosystems to climate change.

In this paper, we develop a method based on graph-cut algorithm to identify alpine grasslines by using multiple sources of remote sensing data, including land cover classification products, Moderate Resolution Imaging Spectroradiometer (MODIS) and Landsat reflectance data, and elevation data. This method would be an important tool for advancing our understanding of the impacts of climate change on alpine ecosystems and for informing conservation and management efforts in alpine regions.

2. Materials and methods

2.1. Overview of the method

Unlike the approaches discussed in the Introduction section, we here use multiple features from multiple satellites to distinguish between alpine grassland and bare land at upper elevations on different mountains across the plateau (Fig. 1).

Because alpine grasslines are located near the border between vegetated and unvegetated land, to reduce data size and computing load, we first used a random forest classifier to identify vegetated and unvegetated areas on the Tibetan plateau on MODIS and Landsat images at the spatial resolution of 250 m. The random forest classifier was trained by using Landsat- and MODIS-based features and land cover types that are consistent across multiple sets of land cover classification products as labels. The use of multiple remotely sensed features and consistent areas in multiple classification products as labels can improve classification accuracy.

Second, we identified 2895 mountains on the plateau on which alpine grasslines were

potentially located based on elevation and a 250-m classification map produced in the above step. Each mountain is covered by vegetation at lower elevations and has unvegetated land at higher elevations. The subsequent steps were carried out separately on individual mountains to avoid the influence of soil and vegetation heterogeneity among mountains.

Third, for each mountain, we defined potential grassline locations as areas at higher elevations where vegetation and unvegetated land were adjacent. In these areas, the vegetation is dominated by alpine grasslands (Shen et al., 2022) (see section 2.5.3). In the potential grassline area on each mountain, we used a linear discriminant analysis (LDA) algorithm to generate from the Landsat-derived features a synthetic feature with a resolution of 30 m that maximized the difference between vegetation and non-vegetation pixels. Next, we used a graph-cut algorithm to detect the alpine vegetation line based on the synthetic feature produced by the LDA. The graph-cut algorithm combines the Otsu and Canny algorithms (see section 2.5.2) and identifies vegetation lines by using the feature value gradient, rather than an artificial threshold, to indicate the presence or absence of vegetation. In more than 99.8% of the areas including vegetation-line pixels, grasslands were the dominant vegetation type; these vegetation lines were therefore interpreted as alpine grasslines.

The resultant alpine grasslines, which had a resolution of 30 m, were validated against visual interpretations of grasslines from drone and PlanetScope images. In the following subsections, we describe the data and methods in detail.

158 *2.2. Datasets*

159 The data used in this study include elevation, land cover products, MODIS reflectance,
160 Landsat reflectance, PlanetScope and drone images, and gridded climate data.

161 The PlanetScope and drone images (Fig. 2) were used to visually interpret alpine grasslines
162 to validate the alpine grasslines extracted from the Landsat data. The PlanetScope images
163 (PlanetTeam, 2020) used in this study consist of 40 blocks, 20 km × 20 km each, acquired in
164 July and August of 2020–2022 with a spatial resolution of 3 m. We further used drones to take
165 orthophotos of 13 blocks of Landsat alpine grasslines in July and August of 2019 and 2022.
166 We set up real-time kinematic base stations to ensure the positional accuracy (latitude and
167 longitude) of the drone images. The spatial resolution of the drone images is between 5 and 10
168 cm. The horizontal and elevational positioning accuracies of the images are 1 m and 5 m,
169 respectively. The alpine grasslines interpreted by using the PlanetScope and drone images have
170 lengths of 8555 km and 114 km, respectively.

171 The other datasets are briefly introduced in the *Supplementary Methods*. Metainformation
172 about these datasets is listed in Table S1.

173

174 *2.3. Identification of vegetated and unvegetated pixels at 250-m resolution*

175 Land covers in each of three classification products (FROM-GLC (Gong et al., 2019; Yu
176 et al., 2022), GlobeLand30 (J. Chen, Ban, & Li, 2014; J. Chen & Chen, 2018), and WorldCover
177 (Zanaga et al., 2022)) were first merged into three types: vegetation, unvegetated land, and
178 water bodies (Table S2). Because there were inconsistencies among the three products (Fig.

179 S1a-c), we selected consistent regions across the three products as labels to train the random
180 forest classifier. The classifier used multiple features (Table S3) calculated from the MODIS
181 and Landsat reflectance data to identify pixels of the three land cover types (vegetation,
182 unvegetated land, and water bodies; Fig. S1d). In this step, all features with a resolution finer
183 than 250 m were resampled to 250 m by using an average aggregating approach. The MODIS
184 data have high temporal resolution and continuous temporal coverage; thus, they could capture
185 temporal land surface dynamics better than the Landsat data. The Landsat data were included
186 because, even resampled to 250 m (the resolution of MODIS), they captured spatial variations
187 better than the MODIS data (Fig. S2) because of differences in the sensors (e.g., different
188 spectral response function and point spread function) and imaging conditions (such as imaging
189 angle) (J. Li et al., 2021). The MODIS- and Landsat-based features and associated quality
190 control methods are introduced in *Supplementary Method* with details.
191
192 *2.4. Identification of mountains with alpine grasslines*
193 Alpine grasslines are located between alpine grasslands and unvegetated land at certain
194 positions on a mountain. Therefore, we identified mountains consisting of vegetated and
195 unvegetated land at higher elevations, based on the SRTM elevation dataset and the 250-m
196 classification map from the above step. To do this, we first idented 8867 mountain peaks with
197 no vegetation coverage. The mountain peak consists of unvegetated pixels with elevation at
198 least 50 m higher than mean of their surrounding areas. In addition to the 250-m classification
199 map, the summer mean NDVI for a mountain peak should be ≤ 0.20, to ensure there was no

vegetation. Details are given in *Supplementary Method*.

For an alpine grassline to exist, there must be vegetation on the lower part of the mountain surrounding the unvegetated mountain peak. To select the mountain peaks surrounded by vegetation, we first defined a 1-km-wide buffer zone surrounding each of the mountain peak identified in the above step. To ensure that there was vegetation in the buffer zone, we excluded the mountain peak if its buffer zone met either of the following two criteria, based on our 250-m classification map and NDVI data: (1) vegetated pixels covered less than 50% of all pixels in the buffer zone; (2) the mean of quality-controlled summer (July–August) MODIS NDVI of the vegetated pixels in the buffer zone during 2015–2021 was less than 0.25. As a result, we identified a total of 2895 mountains that were distributed mostly in alpine grasslands (Shen et al., 2022).

2.5. Identification of alpine grasslines based on Landsat data using a graph-cut algorithm

First, for each mountain, we determined the area where grasslines were potentially located as the boundary area between the vegetated and unvegetated regions using the random classification result (Fig. 3). The boundary area consisted of a 500-m-wide buffer zone from the identified border between vegetated and unvegetated areas in the direction of the unvegetated higher altitudes and a 1500-m-wide buffer zone from the border in the direction of the vegetated lower altitudes (Fig. 3b). Alpine grasslines are defined by the grassland pixels with the highest elevation. Therefore, we used a narrower buffer zone in the unvegetated area than in the vegetated area because the possibility that a grassline exists in the unvegetated area in the upper part of a mountain is extremely low, whereas grasslines might be identified within

a large area below the identified border where the vegetation cover might be low. On the Tibetan Plateau, the dominant vegetation type in these boundary areas is alpine grassland (Shen et al., 2022), as we show in section 2.5.3. We thus use the term grassline rather than vegetation line.

Because of the high heterogeneity of vegetation and soil background across the Tibetan Plateau, we identified alpine grasslines in areas potentially including the grassline separately for each of the mountains identified in section 2.4 based on the features (vegetation indexes) derived from the Landsat reflectance data (Table S3). To do this, we first used the LDA algorithm to maximize the difference in the Landsat-derived features between the vegetated and unvegetated pixels in the area where the grassline was potentially located for each mountain, thereby generating a synthetic feature. Then a graph-cut algorithm was designed to accurately determine the grassline position in each of the areas using the synthetic feature.

2.5.1. Preparation of the synthetic feature from the Landsat vegetation indexes

The LDA algorithm is a supervised linear feature dimensionality reduction algorithm that can be represented as follows:

$$F = \mathbf{w}^T f \quad (1)$$

where f represents the different Landsat-derived features, and F is the linear combination of Landsat-derived features with vector $\mathbf{w}$. Based on the random forest classification, the LDA finds the optimal $\mathbf{w}$ by maximizing the interclass (here, vegetated and unvegetated pixels) difference while simultaneously minimizing the sum of the intraclass variance. Using the

optimal **w**, the original Landsat-derived features (those in Table S3) are transformed into a synthetic feature. Finally, as required by the graph-cut algorithm, we linearly stretched the synthetic feature to 0–255, using the 2nd percentile and the 98th percentile values as minimal and maximal values, respectively. We used the Python scikit-learn 1.1.2 package to implement the LDA algorithm (Pedregosa et al., 2011).

2.5.2. Development of the graph-cut algorithm

Finally, using the synthetic feature with a 30-m spatial resolution obtained by LDA, we segmented the area where grassline was potentially located on each mountain into vegetated pixels and unvegetated pixels. Then, the grasslines were defined as the vegetated pixels on the border between the vegetated and unvegetated areas. To do this, we designed a graph-cut algorithm that combines the Otsu and Canny approaches. In this subsection, we first briefly introduce the Otsu and Canny approaches, and then we describe how these two approaches were integrated in the graph-cut algorithm.

The Otsu algorithm (Otsu, 1979) uses the histogram of the synthetic feature (the colored area in Fig. 4a) as input, and finds a threshold value that classifies the pixels of the synthetic feature as vegetated or unvegetated (Fig. 4b) while maximizing the interclass variance between vegetated and unvegetated pixels. Although this method has been successfully applied to the extraction of treelines and coastlines (He et al., 2020; Tang et al., 2022; Xia Wang, Liu, Ling, Liu, & Fang, 2017), the Otsu algorithm does not consider the spatial texture that dictates a grassline, i.e., a sharp transition from vegetation to non-vegetation. Therefore, the boundary pixels detected by the Otsu algorithm between vegetated and unvegetated pixels indicate the

263 approximate position of the grassline rather than its precise position.

264 The Canny algorithm (Canny, 1986) is an edge detection algorithm that uses spatial
265 gradient information. It can be used to identify boundary pixels with a sharp transition of
266 synthetic feature values on the image; thus, it can potentially be used to determine the position
267 of the grassline. However, the algorithm is so sensitive to spatial texture that it detects all edges,
268 including those between pixels with high and low vegetation coverage (i.e., high and low values
269 of the synthetic feature). Therefore, the Canny algorithm cannot be used alone for grassline
270 detection.

271 In this context, we designed a graph-cut algorithm that combines the advantages of these
272 two algorithms and addresses their limitations. The designed graph-cut algorithm employs the
273 Otsu algorithm to determine the approximate position of the grassline and uses the modified
274 Canny gradient value (Fig. 4c; *Supplementary Method*) to precisely locate the grassline. The
275 new method detects edges that are similar to the results obtained by the Otsu algorithm in terms
276 of their approximate location, but the edge positions are aligned with the pixels with large
277 values of modified Canny gradient (Fig. 4d and e).

278 The graph-cut algorithm considers each synthetic feature image for area where grassline
279 was potentially located on each mountain as a graph, denoted as $G = < v, \varepsilon >$, where v
280 represents the nodes on the graph, which are pixels of the synthetic feature pixels of the image
281 (Boykov, 2004; Y. Li, Sun, Tang, & Shum, 2004) and ε represents the edges between adjacent
282 nodes (i.e., pixels), indicating the relationship between two adjacent pixels of the synthetic
283 feature image. The binarization task can be understood as assigning a label of 1 (vegetated) or

0 (unvegetated) to each pixel $i \in v$; the result of the assignment is denoted as x_i, where $x_i \in$ [vegetated (= 1), unvegetated (= 0)]. The binary result of the synthetic feature image is denoted as $X = \{x_1, \dots, x_i, \dots, x_n\}$, where n is the number of pixels in the area where the grassline was determined to be potentially located in our study. The binarization by the graph-cut algorithm considers both the synthetic feature value of each pixel and the relationship between two adjacent pixels. The goal of the graph-cut algorithm can be understood as finding the optimal X by minimizing the energy function $E(X)$ (Boykov, 2004; Y. Li et al., 2004):

$$E(X) = \sum_{i \in v} E_1(x_i) + \lambda \sum_{(i,j) \in \varepsilon} E_2(x_i, x_j) \qquad (2)$$

where $E_1(x_i)$ represents the cost of pixel i having type x_i, and $E_2(x_i, x_j)$ represents the cost of two adjacent pixels i and j having types x_i and x_j, respectively. When using the graph-cut algorithm, users define different $E_1(x_i)$ and $E_2(x_i, x_j)$ to achieve different segmentation effects. Readers can refer to Boykov (2004) for details about the method for solving the $E(X)$ function. In our study, we used the threshold value of the Otsu algorithm to define $E_1(x_i)$, such that minimizing $E_1(x_i)$ causes X to be close to the result of the Otsu algorithm. Meanwhile, we used the modified Canny gradient to define $E_2(x_i, x_j)$, such that minimizing $E_2(x_i, x_j)$ makes the edges of the obtained X aligned with the pixels with large values of modified-Canny gradient. Thus, minimizing both $E_1(x_i)$ and $E_2(x_i, x_j)$ simultaneously finds X close to the Otsu algorithm result, while the edges of X still coincide the pixels with large values of modified-Canny gradient. The λ parameter is used to control the weight of the edge part in the algorithm. To implement the graph-cut algorithm here, λ was set to 10, and we conducted a sensitivity analysis of the effect of the value of λ on the

accuracy of the grassline identification (see the discussion in section 4.1). Detailed definition of $E_1(x_i)$ and $E_2(x_i, x_j)$ were separately given in the *Supplementary Method*. Using the defined $E_1(x_i)$ and $E_2(x_i, x_j)$, we implemented the graph-cut algorithm with the Pymaxflow package in Python (Boykov, 2004).

After binarization is completed, we defined grasslines as the grassland pixels at the boundary between vegetated and unvegetated ground, and we determined their elevation by using the SRTM data.

2.5.3. Postprocessing

A few unvegetated (vegetated) pixels may scatter inside a vegetated (unvegetated) area. These pixels were not considered to be grassline pixels.

2.5.4. Removing uninterested grasslines and shrubline and treeline

First, we removed grasslines due to ravines or water bodies on the mountain as follows: (1) Grasslines due to a ravine or a water body are characterized by having unvegetated pixels at lower elevations and vegetated pixels at higher elevations. Therefore, for each grassline pixel, we opened a 7 pixel × 7 pixel window and checked the correlation between the elevation and the maximum 30-m Landsat NDVI (Table S3) within the window. We then deleted all grassline pixels that showed a significantly positive correlation ($P < 0.05$). (2) We deleted all grassline pixels (at 30-m resolution) within 250 m of a water pixel in the 250-m random forest classification result.

Second, on the Tibetan Plateau, the boundary between vegetation and high-altitude unvegetated land may represent a shrubline or a treeline. To remove such boundaries, we

326 referred to the FROM-GLC classification product (Table S1) and calculated the dominant
327 vegetation type (the type with the highest proportion) within 3 pixel × 3 pixel and 5 pixel × 5
328 pixel windows with a grassline pixel in the center, respectively. The dominant vegetation type
329 was grassland in more than 99.8% of both the 3 × 3 and 5 × 5 windows (Fig. S4). The grassline
330 pixels with other dominant vegetation types were removed.
331
332 *2.6. Validation*
333 The alpine grasslines identified using the synthetic feature derived from the Landsat
334 images were validated against alpine grasslines visually interpreted on PlanetScope and drone
335 images. To match the Landsat-based grassline, the alpine grasslines from PlanetScope and
336 drone images were first resampled to 30-m resolution by the maximum resampling method.
337 Each pixel of the Landsat-based grasslines was matched with the closest visually interpreted
338 grassline pixel within 2 km (i.e., least distance matching) (Ameztegui, Coll, Brotons, & Ninot,
339 2016). The positional accuracy was quantified by using the mean absolute error, mean error,
340 and R^2 metrics, based on the elevations of alpine grasslines between matched pixels. We also
341 calculated the slope of the linear regression line between the elevation of the grasslines based
342 on Landsat and those based on drone or PlanetScope data across the matched pixels.
343 To test the robustness of our validation, we implemented another two methods for
344 matching the graph-cut grasslines with the visually interpreted grasslines. In one method, these
345 two kinds of grasslines were matched along the normal line of the visually interpreted
346 grasslines (Y. Chen & Kirwan, 2022), and in the other method, along the normal line of the

contour lines (Mathisen et al., 2014). Taking the first method for example, we first set sampling points on the visually interpreted alpine grasslines (resampled to 30-m resolution) every 300 meters. For each sampling point, we determined the normal line of the grasslines with length of 270 m with the sampling point in the center. Then, for each sampling point, we selected the closest graph-cut pixel along the normal line of the grasslines within 2 km. Here, both directions of the normal line were considered. By moving the sampling point along the grasslines, we could finish the matching.

3. Results

The elevations of the alpine grasslines identified from the Landsat data using the graph-cut method were close to those visually interpreted on the drone or PlanetScope images, as shown in the validation results based on least distance matching (Fig. 5). For the Landsat- and drone-based grassline elevations, mean error was 0.4 m, mean absolute error was 22.6 m, R^2 was 0.99, and the slope between the grassline elevations was 0.99 (Fig. 5a). Similarly, validation against PlanetScope-based grasslines showed high grassline identification accuracy (Fig. 5b). Similar results (Fig. S5 and S6) were observed in the validation using the other two methods for matching the graph-cut grasslines and visually interpreted ones. Visual comparison of the Landsat-based and the visually interpreted grasslines also demonstrated the accuracy of the method (Figs. 6 and 7).

The total length of the alpine grasslines identified on the Landsat images was about 419,069 km. In general, the elevation of the alpine grasslines was lower (<4650 m) in the east—

for example, in the Qilian mountains in the northeast and the Hengduan Mountains in the southeast—and higher (>4650 m) in the southwest, for example, in the Kailas Range (Fig. 8a). Across the Tibetan Plateau, the grassline elevation ranged from 4038 m (5th percentile) to 5380 m (95th percentile), with an average elevation of 4841 m and a median elevation of 4841 m (Fig. 8b). Few grasslines occurred below 4000 m (Fig. 8 and Fig. S7). Latitudinally, the elevation increased from about 3715 m at 40°N, to about 5061 m at 30°N, and then decreased to about 4601 m at 27°N (Fig. 8c). Longitudinally, the elevation increased from about 3778 m at 104°E, to about 5367 m at 81°E, and then decreased to about 3911 m at 76°E (Fig. 8d).

4. Discussion

Grasslands are widely distributed in mountain regions of the world, and information about the upper elevation limit of grasslands (alpine grasslines) is of great significance for understanding how the alpine vegetation distribution responds to climate change. However, limited field observations and remote sensing retrievals of alpine grasslines are available. To fill this gap, we developed a method to identify alpine grasslines from multiple types of remote sensing data, including land cover products and MODIS and Landsat reflectance data, able to provide positional information on alpine grasslines at a spatial resolution of 30 m for mountains. Our method uses a graph-cut algorithm to combine the advantages of the Canny and Otsu approaches. Validation against visual interpretations of PlanetScope and drone images indicated that the results had high accuracy.

388 *4.1. Interpretation of the method*

389 First, in this study, we did not determine the grasslines directly from the boundary between
390 grasslands and unvegetated areas at high altitudes in the land cover product; instead, we used
391 the classification product to help identify areas where grasslines were potentially located.
392 Subsequently, precise grassline positions were determined based on the characteristics of a
393 synthetic feature based on multiple vegetation indices derived from Landsat reflectance data.
394 This strategy is expected to avoid the impacts of errors in the classification product and to
395 identify the position of grasslines with higher accuracy. Compared with our method (Figs. 5, 6
396 and 7), the accuracy of grasslines determined directly by using Otsu method and each of the
397 three land cover products was lower when validated against grasslines identified by visual
398 interpretation of the PlanetScope images (Figs. 9, S8 and S9).

399 Second, we identified the alpine grassline separately on each mountain, considering the
400 differences in vegetation characteristics and background land surface among the 2895
401 mountains across the Tibetan Plateau. The 30-m Landsat-based maximum NDVI (Table S3)
402 averaged over the grasslines pixels on each mountain ranged from 0.3 to 0.6 (Fig. S10).
403 Moreover, NDVI values of bare land also show substantial variation across the Tibetan Plateau
404 (Fig. S11). Such spatial variations suggest that it is necessary to identify grasslines separately
405 for each mountain and that using a single threshold NDVI value of 0.10 across the plateau to
406 indicate presence of vegetation could lead to considerable bias (Anderson et al., 2020).

407 Third, when generating the synthetic feature, we used a LDA algorithm to adaptively
408 specify the combinations of features from Landsat-based vegetation indices (Table S3) to

maximize the difference between vegetated and unvegetated pixels for each mountain. The elevations of the alpine grasslines identified by using the synthetic feature were closer to those interpreted from the PlanetScope images than to those identified directly by using a single Landsat-based feature (vegetation index, Table S4).

Finally, the new algorithm combines the Otsu and Canny algorithms in the graph-cut framework for grassline identification. The Otsu algorithm detects grasslines based on the Otsu threshold determined from gray-level histogram information on the synthetic feature, but because it does not consider spatial texture features, it cannot precisely identify the grassline position (Fig. S12a). On the other hand, the Canny algorithm relies entirely on spatial texture features to find edges; consequently, the identified edges include not only those formed by grasslines but also those formed by other sudden changes in the synthetic feature that is not caused by grasslines (Fig. S12b). We designed an energy function *E(X)* based on the graph-cut algorithm that combines the advantages of both algorithms, using the Otsu threshold to determine the approximate spatial position and thereby excluding the non-grassline edges found by the Canny algorithm (Fig. S12c). At the same time, the graph-cut-based grassline position is aligned with the pixels having greater modified Canny gradient values, allowing spatial texture features of the grasslines to be applied. Another advantage of the graph-cut method is that when we do not perform postprocessing on the results of the Otsu method and the graph-cut method, the accuracy of the graph-cut method is higher than the Otsu method (Figs. S13, S14 and S15). This is because our graph-cut method removed most of the non-grassline edges detected by the Otsu algorism (Fig. S15). The graph-cut algorithm adjusts the

weights of the Otsu and Canny positional information through the λ parameter. We tested the sensitivity of the identification of the position of the alpine grassline to the λ parameter (Fig. S16). We found that, given that the approximate grassline position had been determined by the Otsu threshold, changes in the λ value caused only marginal variations in MAE and R^2 between graph-cut-based and PlanetScope-based grasslines.

4.2. Perspectives

Clearly, the identification of grassline positions depends on the spatial resolution of the remote sensing data. Taking into account data availability, our method relies mainly on 30-m resolution Landsat data. Although the grasslines identified by using the Landsat data and those visually interpreted from drone and PlanetScope images are close to each other, data with higher spatial resolution than Landsat are needed when higher accuracy is required for grassline identification. Additionally, when the transition from vegetated to unvegetated areas is relatively gradual, it is difficult to visually interpret the position of the grasslines on high- and medium-resolution images or even in a field survey. Resolution of this problem requires further efforts on the part of botanists and ecologists to define grasslines in areas where the transition is gradual.

We proposed the method for identifying alpine grasslines on the Tibetan Plateau. However, the Tibetan Plateau is characterized by high geographic and vegetation diversity, and we did not set critical specific regional thresholds. Therefore, our method should also be applicable for identifying alpine grasslines in other regions, such as the Andes Mountains of South

America. Similarly, for grasslines not related to elevation, such as those at the boundary between grasslands and sandy lands, our method can also be a valuable reference. Moreover, our method is potentially applicable to the detection of treelines and shrublines in alpine areas. Finally, Landsat data archives cover more than 40 years; thus, our method can be used to identify historical positions of alpine grasslines, thereby laying a foundation for studying their response to climate change.

5. Conclusion

Taking the Tibetan Plateau as an example, we proposed a novel method for remotely sensing the position of alpine grasslines at a spatial resolution of 30 m at large scale. We first identified 2895 mountains potentially having alpine grasslines. We then produced a synthetic feature from multiple vegetation indices calculated from Landsat reflectance data. Next, we combined the Otsu and Canny approaches in the framework of a graph-cut algorithm to identify the position of alpine grasslines with respect to the synthetic feature at a spatial resolution of 30 m. Validation against visually interpreted alpine grasslines in PlanetScope and drone images suggests that the accuracy of the resultant Landsat-based grasslines is high. Across the Tibetan Plateau, the elevation of alpine grasslines showed high spatial variability, ranging from 4038 m (5th percentile) to 5380 m (95th percentile). Our study provides a method for retrieving alpine grasslines by using remote sensing data and lays an important foundation for studying their response to climate change. This method is also referenceable for detecting other borders such as treelines and horizontal grasslines.

Acknowledgements

This research was supported by the following funding: the Second Tibetan Plateau Scientific Expedition and Research Program (grant no. 2019QZKK0405, 2019QZKK0106 and 20190ZKK0307), the Fundamental Research Funds for the Central Universities, the Japan Society for the Promotion of Science (JSPS) KAKENHI Grant Number 23K18517, and the Top-Notch Young Talents Program of China (to M Shen).

Author contributions

Licong Liu: Methodology, Visualization and Writing - Original Draft; **Miaogen Shen**: Conceptualization, Supervision and Writing - Review & Editing; **Jin Chen:** Supervision and Writing - Review & Editing; **Xuehong Chen, Ruyin Cao, Xin Cao, Xihong Cui, Wei Yang, Xiaolin Zhu** and **Le Li**: Writing - Review & Editing; **Yanhong Tang**: Conceptualization, Writing - Review & Editing;

Conflict of Interest Statement

The authors declare no competing interests.

Data Availability Statement

The Landsat 8 Level 2 Collection 2 Tier 1 data, MOD09Q1 v061 data, MOD09A1 v 061, SRTM data and ESA WorldCover 10m v200 classification data are available at:

https://earthengine.google.com/. The GlobeLand30 classification data is available at: http://www.globallandcover.com. FROM-GLC 2017v1 classification data is available at: http://data.ess.tsinghua.edu.cn. The drone images are available at http://dx.doi.org/10.17632/phjgbzcfh9.1. The PlanetScope images are available at: https://www.planet.com/explorer/. The Landsat alpine grasslines and visually interpreted drone and PlanetScope alpine grasslines are available at https://ee-licongliu.projects.earthengine.app/view/alpine-grasslines.

Figure legends

Figure 1. Overview of the method for mapping alpine grasslines.

Figure 2. The spatial distribution of sites validated against drone and PlanetScope images.

Figure 3. Schematic diagram illustrating how the area potentially including the grassline was determined: (a) 250-m classification map; (b) identified area within which the grassline is potentially located.

Figure 4. The process of identifying alpine grasslines from the synthetic feature using a graph-cut algorithm. (a) The synthetic feature transformed from Landsat-based features (Table S3) by LDA at 30-m spatial resolution. Greener areas represent pixels with higher vegetation coverage. (b) Binarization of the synthetic feature by the Otsu algorithm. The white and green areas represent unvegetated and vegetated pixels, respectively. (c) The modified Canny gradient from the synthetic feature. (d and e) The edge detection result (alpine grassline) of the graph-cut

algorithm combining the Otsu and modified Canny gradient, shown on the synthetic feature and PlanetScope RGB images, respectively. The red square in (a) indicate the area for which an enlarged view was presented in Fig. S3.

Figure 5. Validation of the alpine grasslines identified on the Landsat images using graph-cut method. Comparison between elevations of alpine grasslines identified by using the graph-cut method from Landsat data and those visually interpreted from (a) drone or (b) PlanetScope data. Metrics are ME, mean error; MAE, mean absolute error; and R^2. The black lines are the linear regression lines between elevations of Landsat-based grasslines and those based on drone or PlanetScope data. The dashed line is the 1:1 line. The graph-cut grasslines were matched with the visually interpreted grasslines using the least distance matching method.

Figure 6. Landsat-based grasslines shown on drone images of four cases: (a) High vegetation coverage, (b) low vegetation coverage, (c) steep vegetation coverage gradient (i.e., a sudden transition from vegetation to bare land), and (d) gentle vegetation coverage gradient (i.e., a gradual transition from vegetation to bare land). The latitude and longitude of the top-left pixel of each image are shown at the top of each panel.

Figure 7. Landsat-based grasslines on PlanetScope RGB images, Landsat maximum NDVI images, and PlanetScope NDVI images for four cases: (a) High vegetation coverage, (b) low vegetation coverage, (c) sharp vegetation coverage gradient (i.e., a sudden transition from vegetation to bare land), and (d) gentle vegetation coverage gradient (i.e., a gradual transition from vegetation to bare land). The latitude and longitude of the top-left pixel of each image are shown at the top of each panel.

Figure 8. (a) The spatial pattern of the grassline elevations based on Landsat data. (b) Histogram of grassline elevations. Changes in the grassline elevation along (c) latitude and (d) longitude. The black lines represent the mean grassline elevation within 0.1° intervals of latitude or longitude.

Figure 9. Comparisons between visually interpreted alpine grasslines and alpine grasslines identified directly by using the Otsu method and three land cover products: (a, b) Otsu, (c, d) WorldCover, (e, f) GlobeLand30, and (g, h) FROM-GLC. In each land cover product, the grassline was determined as the grassland pixels at the boundary between vegetated and unvegetated pixels. Metrics are ME, MAE, and R^2, and the black lines show the slope of the linear regression between the elevation of Landsat-based grasslines and that of grasslines based on drone and PlanetScope data. The dashed line indicates a 1:1 correspondence.

References

Ameztegui, A., Coll, L., Brotons, L., & Ninot, J. M. (2016). Land-use legacies rather than climate change are driving the recent upward shift of the mountain tree line in the Pyrenees. *Global Ecology and Biogeography, 25*(3), 263-273. doi:10.1111/geb.12407

An, S., Zhu, X., Shen, M., Wang, Y., Cao, R., Chen, X., . . . Tang, Y. (2018). Mismatch in elevational shifts between satellite observed vegetation greenness and temperature isolines during 2000-2016 on the Tibetan Plateau. *Glob Chang Biol, 24*(11), 5411-5425. Retrieved from https://www.ncbi.nlm.nih.gov/pubmed/30156039. doi:10.1111/gcb.14432

Anderson, K., Fawcett, D., Cugulliere, A., Benford, S., Jones, D., & Leng, R. (2020). Vegetation expansion in the subnival Hindu Kush Himalaya. *Glob Chang Biol, 26*(3), 1608-1625. Retrieved from https://www.ncbi.nlm.nih.gov/pubmed/31918454. doi:10.1111/gcb.14919

Bobrowski, M., Gerlitz, L., & Schickhoff, U. (2017). Modelling the potential distribution of Betula utilis in the Himalaya. *Global Ecology and Conservation, 11*, 69-83. doi:10.1016/j.gecco.2017.04.003

Boykov, Y. K., Vladimir. (2004). An experimental comparison of min-cut/max-flow algorithms

for energy minimization in vision. *IEEE transactions on pattern analysis and machine intelligence, 26*(9), 1124-1137.

Canny, J. (1986). A computational approach to edge detection. *IEEE transactions on pattern analysis and machine intelligence*(6), 679-698.

Chapin, F. S., 3rd, McGuire, A. D., Randerson, J., Pielke, R., Baldocchi, D., Hobbie, S. E., . . . Running, S. W. (2000). Arctic and boreal ecosystems of western North America as components of the climate system. *Glob Chang Biol, 6*(S1), 211-223. Retrieved from https://www.ncbi.nlm.nih.gov/pubmed/35026938. doi:10.1046/j.1365-2486.2000.06022.x

Chen, I. C., Hill, J. K., Ohlemuller, R., Roy, D. B., & Thomas, C. D. (2011). Rapid range shifts of species associated with high levels of climate warming. *Science, 333*(6045), 1024-1026. Retrieved from https://www.ncbi.nlm.nih.gov/pubmed/21852500. doi:10.1126/science.1206432

Chen, J., Ban, Y., & Li, S. (2014). Open access to Earth land-cover map. *Nature, 514*(7523), 434-434. Retrieved from https://doi.org/10.1038/514434c. doi:10.1038/514434c

Chen, J., & Chen, J. (2018). GlobeLand30: Operational global land cover mapping and big-data analysis. *Science China Earth Sciences, 61*(10), 1533-1534. doi:10.1007/s11430-018-9255-3

Chen, Y., & Kirwan, M. L. (2022). A phenology- and trend-based approach for accurate mapping of sea-level driven coastal forest retreat. *Remote Sensing of Environment, 281*. doi:10.1016/j.rse.2022.113229

Compagnoni, A., Levin, S., Childs, D. Z., Harpole, S., Paniw, M., Romer, G., . . . Knight, T. M. (2021). Herbaceous perennial plants with short generation time have stronger responses to climate anomalies than those with longer generation time. *Nat Commun, 12*(1), 1824. Retrieved from https://www.ncbi.nlm.nih.gov/pubmed/33758189. doi:10.1038/s41467-021-21977-9

Cong, N., Shen, M., Yang, W., Yang, Z., Zhang, G., & Piao, S. (2017). Varying responses of vegetation activity to climate changes on the Tibetan Plateau grassland. *International Journal of Biometeorology, 61*, 1433-1444.

Crimmins, S. M., Dobrowski, S. Z., Greenberg, J. A., Abatzoglou, J. T., & Mynsberge, A. R. (2011). Changes in climatic water balance drive downhill shifts in plant species' optimum elevations. *Science, 331*(6015), 324-327. Retrieved from https://www.ncbi.nlm.nih.gov/pubmed/21252344. doi:10.1126/science.1199040

Dolezal, J., Dvorsky, M., Kopecky, M., Liancourt, P., Hiiesalu, I., Macek, M., . . . Schweingruber, F. (2016). Vegetation dynamics at the upper elevational limit of vascular plants in Himalaya. *Sci Rep, 6*, 24881. Retrieved from https://www.ncbi.nlm.nih.gov/pubmed/27143226. doi:10.1038/srep24881

Gong, P., Liu, H., Zhang, M., Li, C., Wang, J., Huang, H., . . . Song, L. (2019). Stable classification with limited sample: transferring a 30-m resolution sample set collected in 2015 to mapping 10-m resolution global land cover in 2017. *Sci Bull (Beijing), 64*(6), 370-373. Retrieved from https://www.ncbi.nlm.nih.gov/pubmed/36659725. doi:10.1016/j.scib.2019.03.002

606 Hansen, M. C., Potapov, P. V., Moore, R., Hancher, M., Turubanova, S. A., Tyukavina, A., . . .
607 Loveland, T. R. (2013). High-resolution global maps of 21st-century forest cover
608 change. *Science, 342*(6160), 850-853.
609 He, W., Ye, C., Sun, J., Xiong, J., Wang, J., & Zhou, T. (2020). Dynamics and Drivers of the
610 Alpine Timberline on Gongga Mountain of Tibetan Plateau-Adopted from the Otsu
611 Method on Google Earth Engine. *Remote Sensing, 12*(16). doi:10.3390/rs12162651
612 Huang, N., He, J. S., Chen, L., & Wang, L. (2018). No upward shift of alpine grassland
613 distribution on the Qinghai-Tibetan Plateau despite rapid climate warming from 2000
614 to 2014. *Sci Total Environ, 625*, 1361-1368. Retrieved from
615 https://www.ncbi.nlm.nih.gov/pubmed/29996433. doi:10.1016/j.scitotenv.2018.01.034
616 Kelly, A. E., & Goulden, M. L. (2008). Rapid shifts in plant distribution with recent climate
617 change. *Proceedings of the national academy of sciences, 105*(33), 11823-11826.
618 Lenoir, J., Gégout, J.-C., Marquet, P. A., de Ruffray, P., & Brisse, H. (2008). A significant
619 upward shift in plant species optimum elevation during the 20th century. *Science,*
620 *320*(5884), 1768-1771.
621 Li, J., Li, Y., Cai, R., He, L., Chen, J., & Plaza, A. (2021). Enhanced spatiotemporal fusion via
622 MODIS-like images. *IEEE Transactions on Geoscience and Re*
623 *mote Sensing, 60*, 1-17.
624 Li, Y., Sun, J., Tang, C.-K., & Shum, H.-Y. (2004). Lazy snapping. *ACM Transactions on*
625 *Graphics (ToG), 23*(3), 303-308.
626 Liang, E., Wang, Y., Piao, S., Lu, X., Camarero, J. J., Zhu, H., . . . Penuelas, J. (2016). Species
627 interactions slow warming-induced upward shifts of treelines on the Tibetan Plateau.
628 *Proc Natl Acad Sci U S A, 113*(16), 4380-4385. Retrieved from
629 https://www.ncbi.nlm.nih.gov/pubmed/27044083. doi:10.1073/pnas.1520582113
630 Mathisen, I. E., Mikheeva, A., Tutubalina, O. V., Aune, S., Hofgaard, A., & Rocchini, D. (2014).
631 Fifty years of tree line change in the Khibiny Mountains, Russia: advantages of
632 combined remote sensing and dendroecological approaches. *Applied Vegetation*
633 *Science, 17*(1), 6-16. doi:10.1111/avsc.12038
634 Montandon, L., & Small, E. (2008). The impact of soil reflectance on the quantification of the
635 green vegetation fraction from NDVI. *Remote Sensing of Environment, 112*(4), 1835-
636 1845. doi:10.1016/j.rse.2007.09.007
637 Myers-Smith, I. H., Forbes, B. C., Wilmking, M., Hallinger, M., Lantz, T., Blok, D., . . . Hik,
638 D. S. (2011). Shrub expansion in tundra ecosystems: dynamics, impacts and research
639 priorities. *Environmental Research Letters, 6*(4). doi:10.1088/1748-9326/6/4/045509
640 Otsu, N. (1979). A threshold selection method from gray-level histograms. *IEEE transactions*
641 *on systems, man, and cybernetics, 9*(1), 62-66.
642 Pedregosa, F., Varoquaux, G., Gramfort, A., Michel, V., Thirion, B., Grisel, O., . . . Dubourg,
643 V. (2011). Scikit-learn: Machine learning in Python. *the Journal of machine Learning*
644 *research, 12*, 2825-2830.
645 PlanetTeam. (2020). Planet imagery product specifications. Available online.
646 https://www.planet.com/products/. .
647 Shen, M., Wang, S., Jiang, N., Sun, J., Cao, R., Ling, X., . . . Fu, B. (2022). Plant phenology

changes and drivers on the Qinghai–Tibetan Plateau. *Nature Reviews Earth & Environment, 3*(10), 633-651. doi:10.1038/s43017-022-00317-5

Tang, W., Zhao, C., Lin, J., Jiao, C., Zheng, G., Zhu, J., . . . Han, X. (2022). Improved Spectral Water Index Combined with Otsu Algorithm to Extract Muddy Coastline Data. *Water, 14*(6). doi:10.3390/w14060855

Wang, C., Guo, H., Zhang, L., Liu, S., Qiu, Y., & Sun, Z. (2015). Assessing phenological change and climatic control of alpine grasslands in the Tibetan Plateau with MODIS time series. *Int J Biometeorol, 59*(1), 11-23. Retrieved from https://www.ncbi.nlm.nih.gov/pubmed/24682528. doi:10.1007/s00484-014-0817-5

Wang, X., Liu, Y., Ling, F., Liu, Y., & Fang, F. (2017). Spatio-Temporal Change Detection of Ningbo Coastline Using Landsat Time-Series Images during 1976–2015. *ISPRS International Journal of Geo-Information, 6*(3). doi:10.3390/ijgi6030068

Wang, X., Wang, T., Xu, J., Shen, Z., Yang, Y., Chen, A., . . . Piao, S. (2022). Enhanced habitat loss of the Himalayan endemic flora driven by warming-forced upslope tree expansion. *Nat Ecol Evol, 6*(7), 890-899. Retrieved from https://www.ncbi.nlm.nih.gov/pubmed/35654898. doi:10.1038/s41559-022-01774-3

Wang, Y., Liang, E., Lu, X., Camarero, J. J., Babst, F., Shen, M., & Peñuelas, J. (2021). Warming‐induced shrubline advance stalled by moisture limitation on the Tibetan Plateau. *Ecography, 44*(11), 1631-1641. doi:10.1111/ecog.05845

Yu, L., Du, Z., Dong, R., Zheng, J., Tu, Y., Chen, X., . . . Gong, P. (2022). FROM-GLC Plus: toward near real-time and multi-resolution land cover mapping. *GIScience & Remote Sensing, 59*(1), 1026-1047. doi:10.1080/15481603.2022.2096184

Zanaga, D., Van De Kerchove, R., Daems, D., De Keersmaecker, W., Brockmann, C., Kirches, G., . . . Fritz, S. (2022). ESA WorldCover 10 m 2021 v200. doi:10.5281/zenodo.7254221

Zhang, W., Miller, P. A., Smith, B., Wania, R., Koenigk, T., & Döscher, R. (2013). Tundra shrubification and tree-line advance amplify arctic climate warming: results from an individual-based dynamic vegetation model. *Environmental Research Letters, 8*(3). doi:10.1088/1748-9326/8/3/034023

Zong, S., Lembrechts, J. J., Du, H., He, H. S., Wu, Z., Li, M., & Rixen, C. (2022). Upward range shift of a dominant alpine shrub related to 50 years of snow cover change. *Remote Sensing of Environment, 268*. doi:10.1016/j.rse.2021.112773

Zou, L., Tian, F., Liang, T., Eklundh, L., Tong, X., Tagesson, T., . . . Fensholt, R. (2023). Assessing the upper elevational limits of vegetation growth in global high-mountains. *Remote Sensing of Environment, 286*. doi:10.1016/j.rse.2022.113423

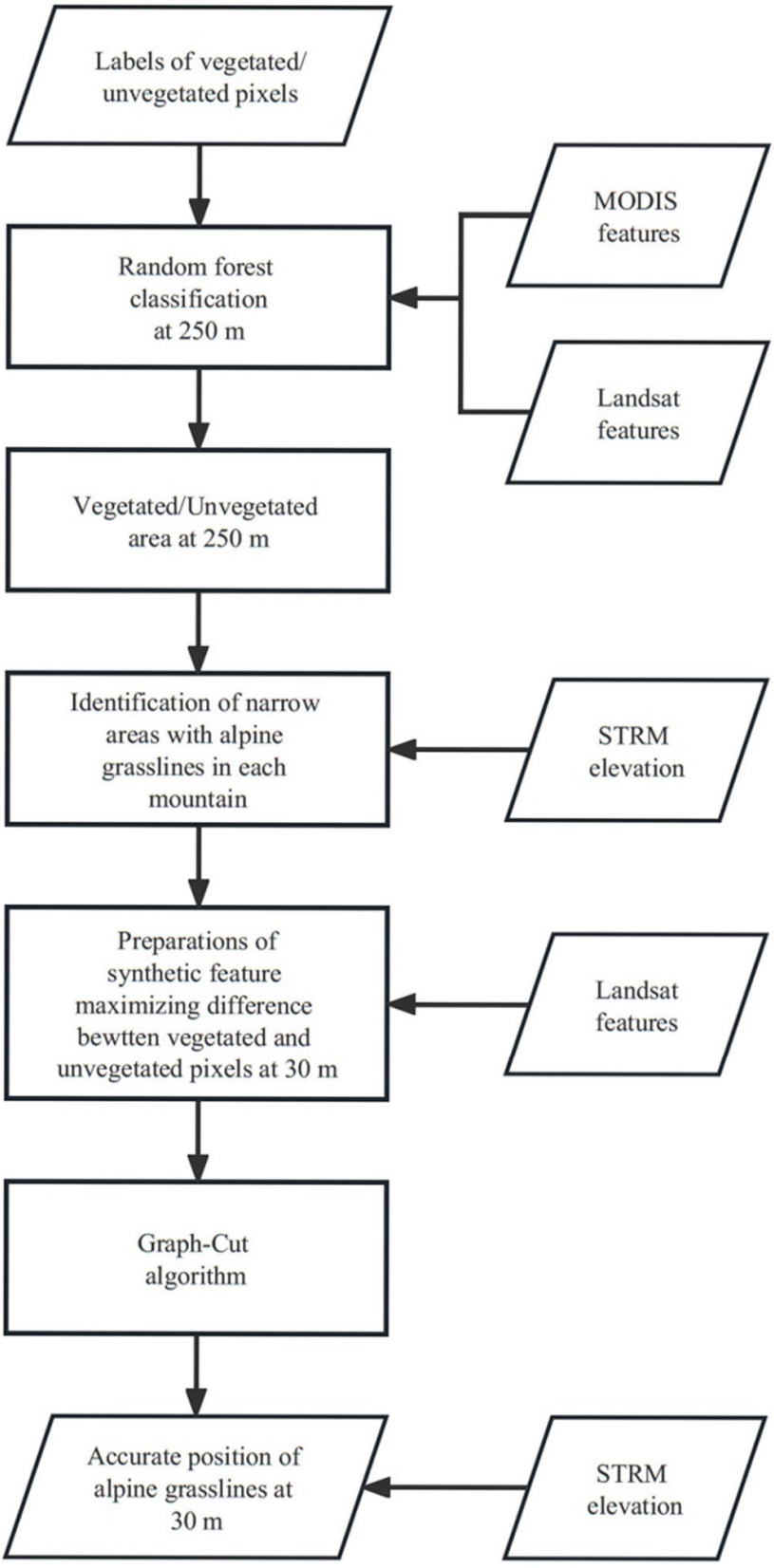
Labels of vegetated/ unvegetated pixels
MODIS features
Random forest classification at 250 m
Landsat features
Vegetated/Unvegetated area at 250 m
Identification of narrow areas with alpine grasslines in each mountain
STRM elevation
Preparations of synthetic feature maximizing difference bewtten vegetated and unvegetated pixels at 30 m
Landsat features
Graph-Cut algorithm
Accurate position of alpine grasslines at 30 m
STRM elevation

687

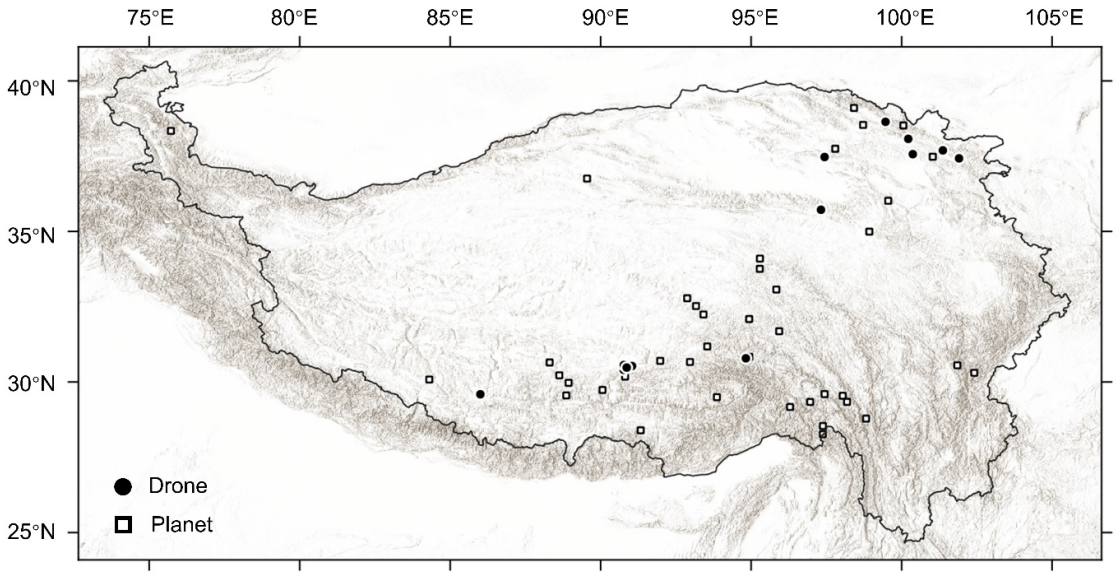
75°E
80°E
85°E
90°E
95°E
100°E
105°E
40°N
35°N
30°N
25°N
Drone
Planet

688

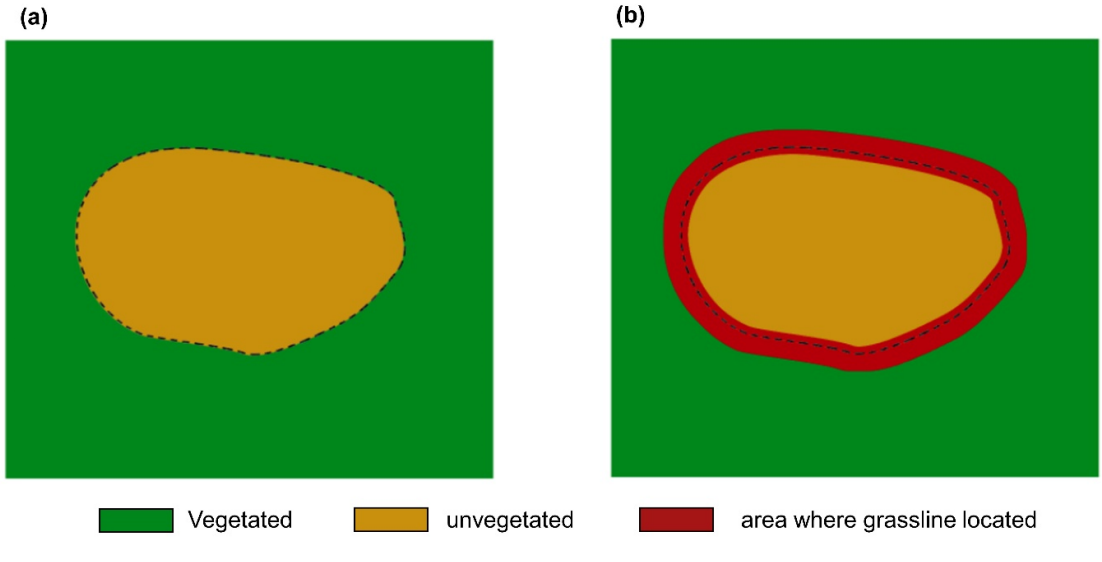
(a)
(b)
Vegetated
unvegetated
area where grassline located

689

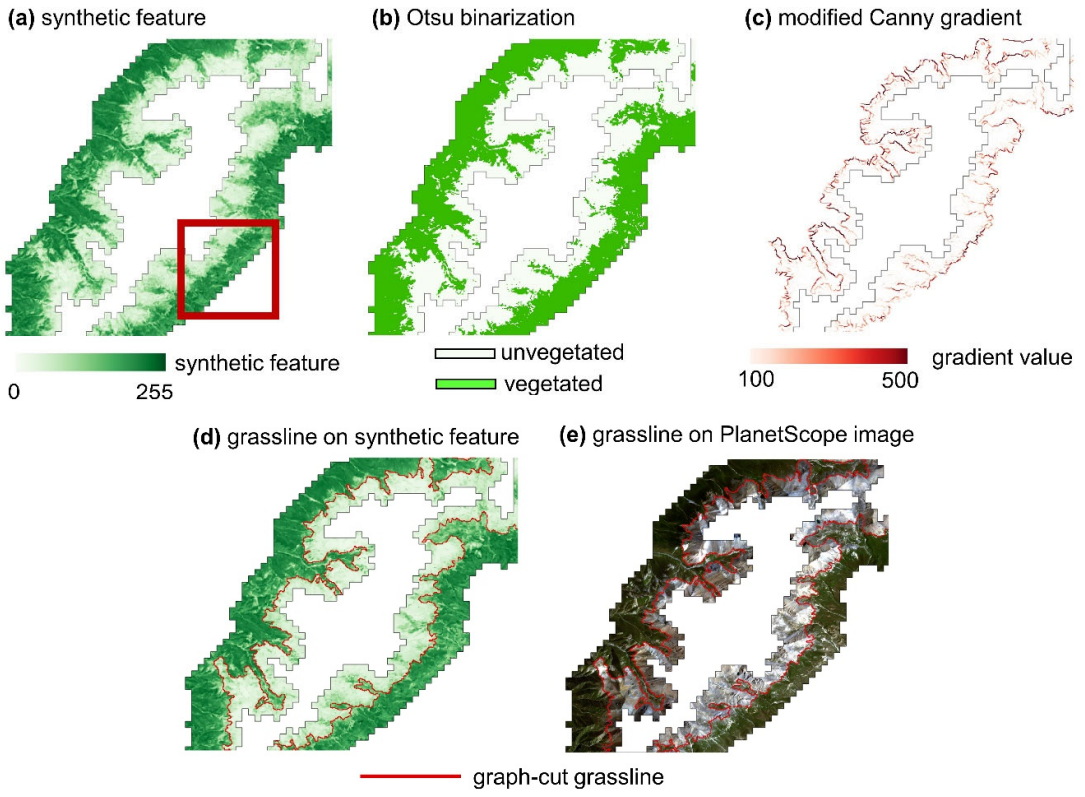
(a) synthetic feature
(b) Otsu binarization
(c) modified Canny gradient
synthetic feature
0
255
unvegetated
vegetated
gradient value
100
500
(d) grassline on synthetic feature
(e) grassline on PlanetScope image
graph-cut grassline

690

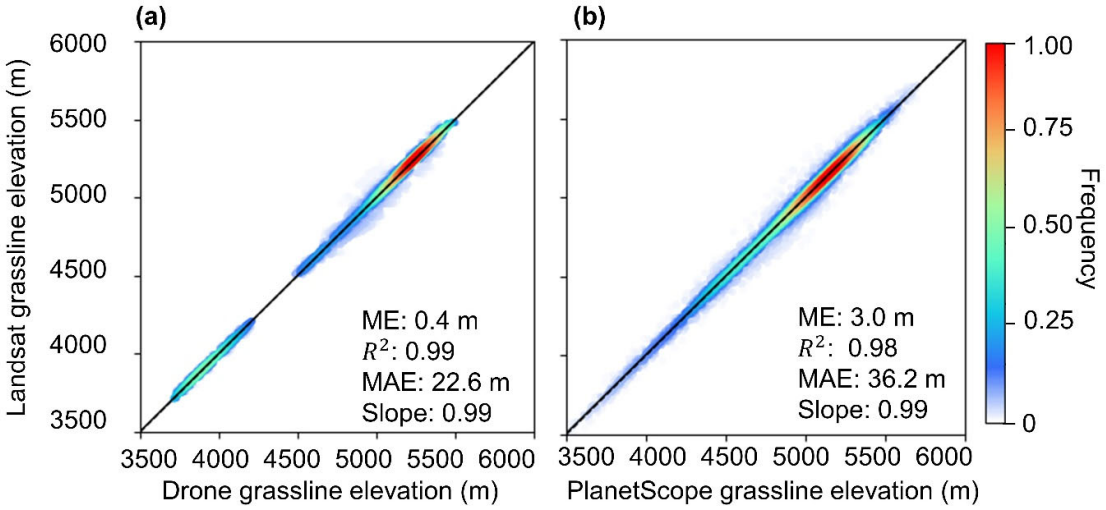
(a)
(b)
Landsat grassline elevation (m)
6000
5500
5000
4500
4000
3500
ME: 0.4 m
R^2: 0.99
MAE: 22.6 m
Slope: 0.99
ME: 3.0 m
R^2: 0.98
MAE: 36.2 m
Slope: 0.99
3500 4000 4500 5000 5500 6000
Drone grassline elevation (m)
PlanetScope grassline elevation (m)
1.00
0.75
0.50
0.25
0
Frequency

691

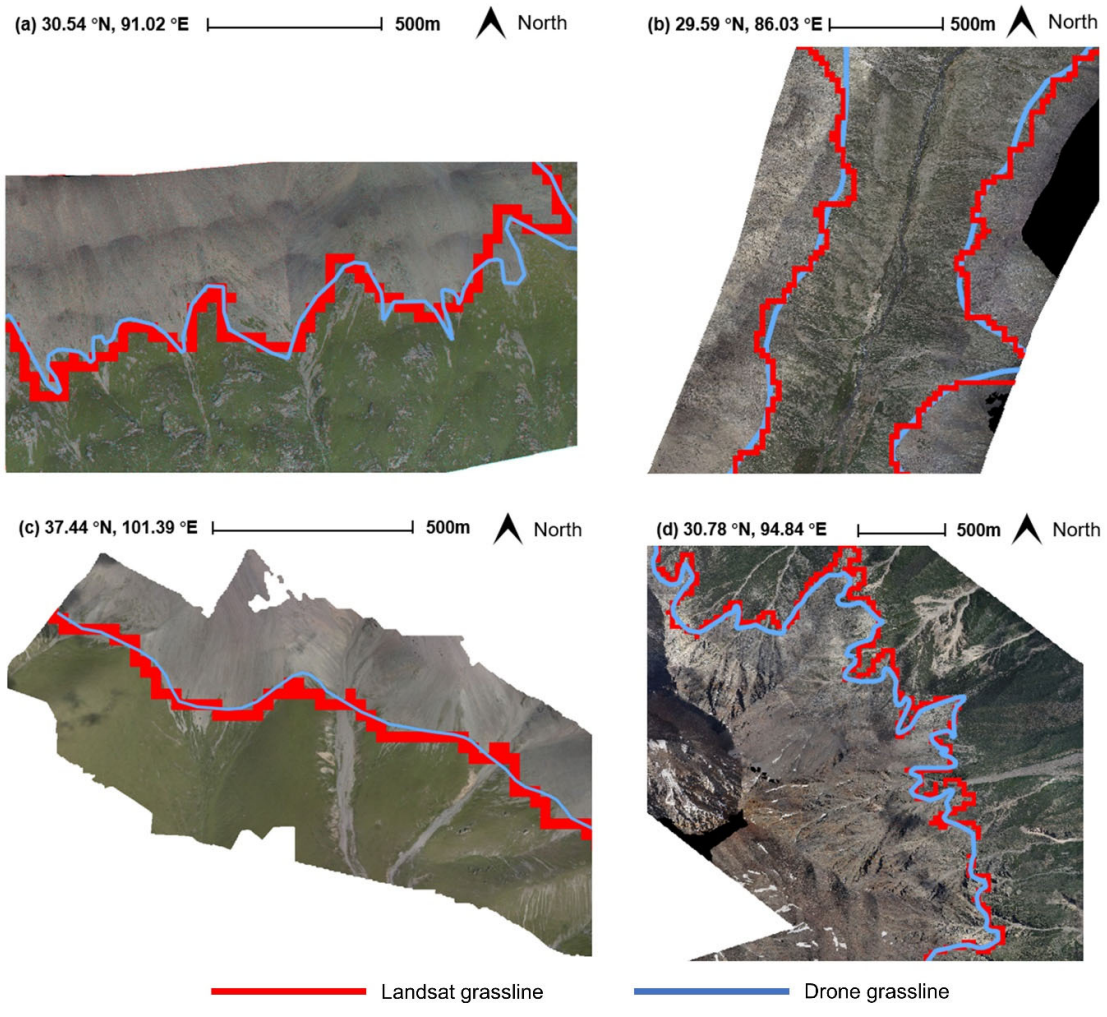
(a) 30.54 °N, 91.02 °E
500m
North
(b) 29.59 °N, 86.03 °E
500m
North
(c) 37.44 °N, 101.39 °E
500m
North
(d) 30.78 °N, 94.84 °E
500m
North
Landsat grassline
Drone grassline

692

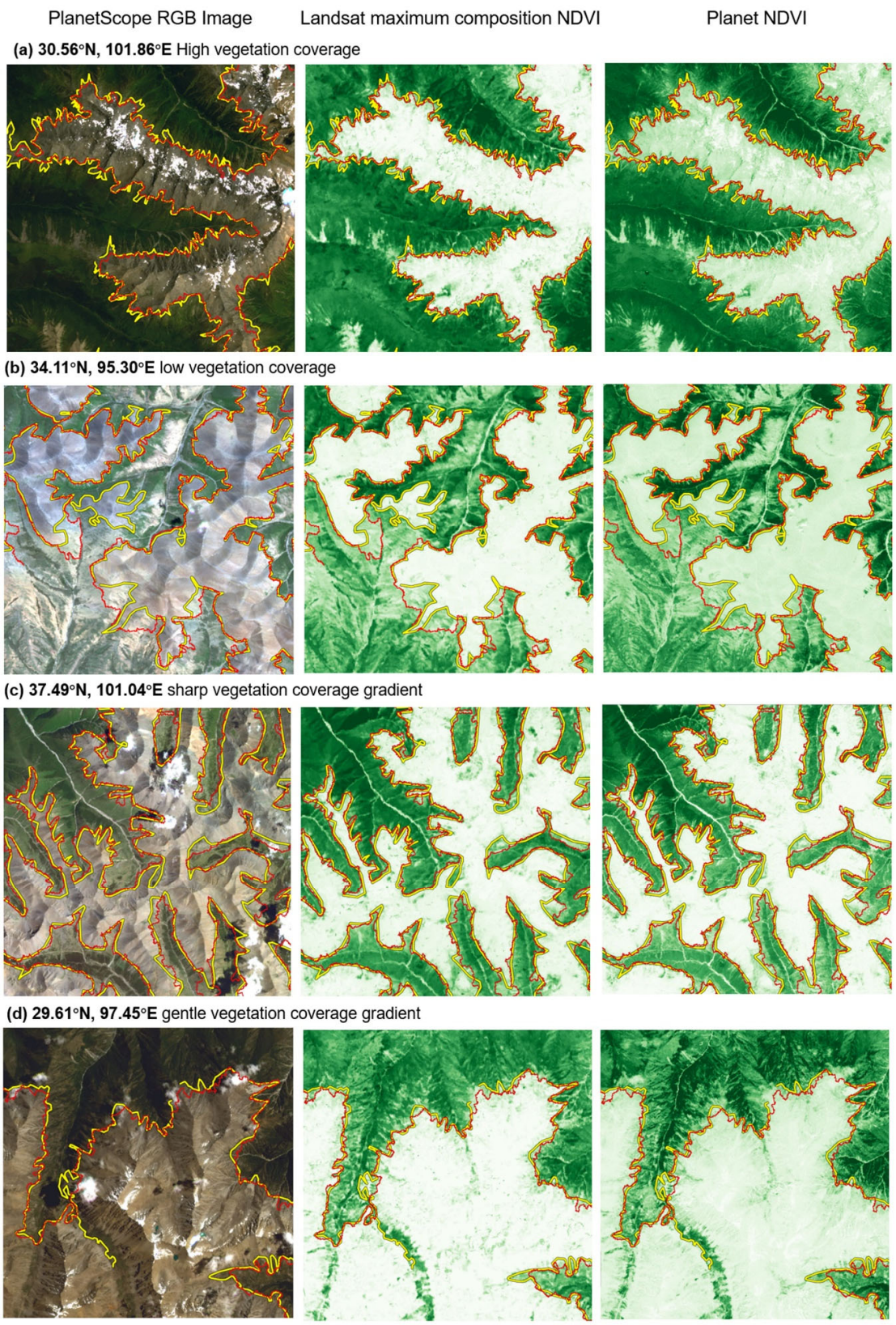
PlanetScope RGB Image
Landsat maximum composition NDVI
Planet NDVI
(a) 30.56°N, 101.86°E High vegetation coverage
(b) 34.11°N, 95.30°E low vegetation coverage
(c) 37.49°N, 101.04°E sharp vegetation coverage gradient
(d) 29.61°N, 97.45°E gentle vegetation coverage gradient

693

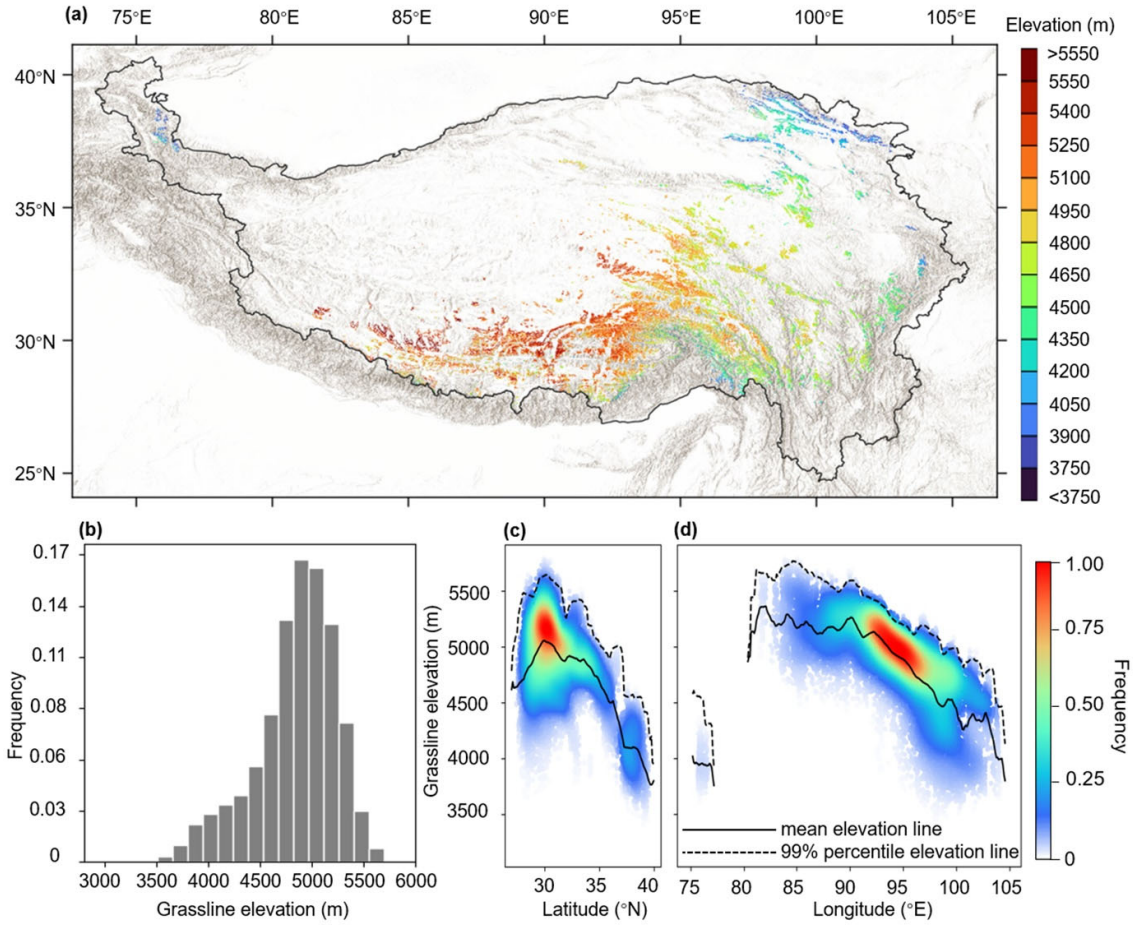
(a)
75°E
80°E
85°E
90°E
95°E
100°E
105°E
40°N
35°N
30°N
25°N
Elevation (m)
>5550
5550
5400
5250
5100
4950
4800
4650
4500
4350
4200
4050
3900
3750
<3750
(b)
Frequency
0.17
0.14
0.11
0.08
0.06
0.03
0
3000
3500
4000
4500
5000
5500
6000
Grassline elevation (m)
(c)
Grassline elevation (m)
5500
5000
4500
4000
3500
30
35
40
Latitude (°N)
(d)
mean elevation line
99% percentile elevation line
75
80
85
90
95
100
105
Longitude (°E)
1.00
0.75
0.50
0.25
0
Frequency

694

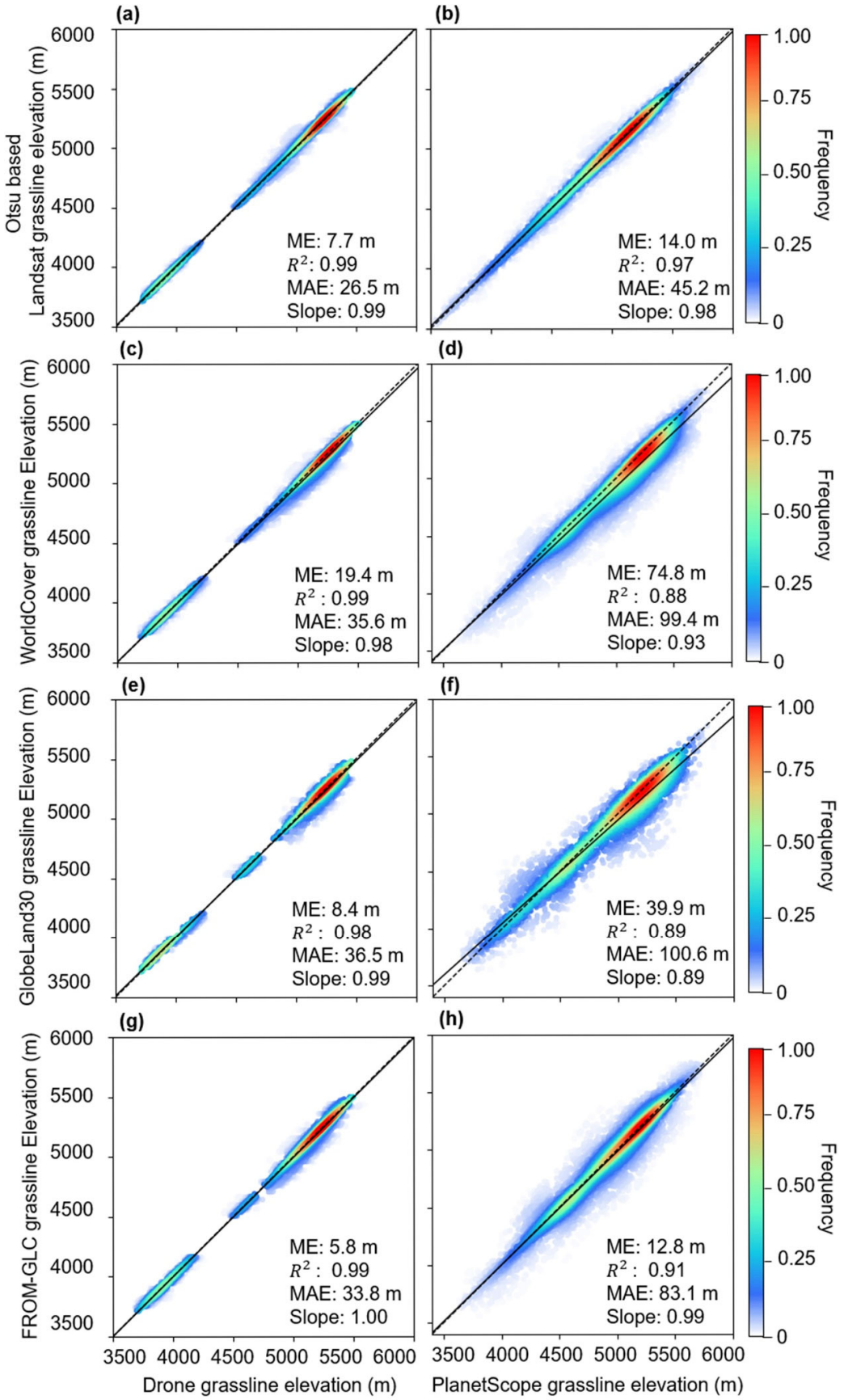
(a)
(b)
(c)
(d)
(e)
(f)
(g)
(h)
Otsu based Landsat grassline elevation (m)
WorldCover grassline Elevation (m)
GlobeLand30 grassline Elevation (m)
FROM-GLC grassline Elevation (m)
ME: 7.7 m
R^2: 0.99
MAE: 26.5 m
Slope: 0.99
ME: 14.0 m
R^2: 0.97
MAE: 45.2 m
Slope: 0.98
ME: 19.4 m
R^2 : 0.99
MAE: 35.6 m
Slope: 0.98
ME: 74.8 m
R^2 : 0.88
MAE: 99.4 m
Slope: 0.93
ME: 8.4 m
R^2 : 0.98
MAE: 36.5 m
Slope: 0.99
ME: 39.9 m
R^2 : 0.89
MAE: 100.6 m
Slope: 0.89
ME: 5.8 m
R^2 : 0.99
MAE: 33.8 m
Slope: 1.00
ME: 12.8 m
R^2 : 0.91
MAE: 83.1 m
Slope: 0.99
3500 4000 4500 5000 5500 6000
Drone grassline elevation (m)
PlanetScope grassline elevation (m)
Frequency
1.00
0.75
0.50
0.25
0

695